CONF-960412--

WAPD-T-3096

CORROSION FATIGUE CRACK GROWTH IN CLAD LOW-ALLOY STEELS: PART II: WATER FLOW RATE EFFECTS IN HIGH-SULFUR PLATE STEEL

L. A. James, H. B. Lee, G. L. Wire, S. R. Novak, and W. H. Cullen

U.S. Department of Energy Contract DE-AC11-93PN38195

Proposed for Submittal to the
Journal of Pressure Vessel Technology

BETTIS ATOMIC POWER LABORATORY PITTSBURGH, PENNSYLVANIA 15122-0079

Operated for the U.S. Department of Energy
by WESTINGHOUSE ELECTRIC CORPORATION

WAPD-T-3096

CORROSION FATIGUE CRACK GROWTH IN CLAD LOW-ALLOY STEELS: PART II, WATER FLOW RATE EFFECTS IN HIGH-SULFUR PLATE STEEL

L. A. James*, H. B. Lee, G. L. Wire, and S. R. Novak
Bettis Atomic Power Laboratory
West Mifflin, PA 15122
and
W. H. Cullen
Materials Engineering Associates
Lanham, MD 20706

ABSTRACT

Corrosion fatigue crack propagation tests were conducted on a high-sulfur ASTM A302-B plate steel overlaid with weld-deposited Alloy EN82H cladding. The specimens featured semi-elliptical surface cracks penetrating approximately 6.3 mm of cladding into the underlying steel. The initial crack sizes were relatively large with surface lengths of 22.8-27.3 mm, and depths of 10.5-14.1 mm. The experiments were initiated in a quasi-stagnant low-oxygen (O_2 < 10 ppb) aqueous environment at 243°C, under loading conditions (ΔK, R, cyclic frequency) conducive to environmentally-assisted cracking (EAC) under quasi-stagnant conditions. Following fatigue testing under quasi-stagnant conditions where EAC was observed, the specimens were then fatigue tested under conditions where active water flow of either 1.7 m/sec. or 4.7 m/sec. was applied parallel to the crack. Earlier experiments on unclad surface-cracked specimens of the same steel exhibited EAC under quasi-stagnant conditions, but water flow rates at 1.7 m/sec. and 5.0 m/sec. parallel to the crack mitigated EAC. In the present experiments on clad specimens, water flow at approximately the same as the lower of these velocities did not mitigate EAC, and a free stream velocity approximately the same as the higher of these velocities resulted in sluggish mitigation of EAC. The lack of robust EAC mitigation was attributed to the greater crack surface roughness in the cladding interfering with flow induced within the crack cavity. An analysis employing the computational fluid dynamics code, FIDAP, confirmed that frictional forces associated with the cladding crack surface roughness reduced the interaction between the free stream and the crack cavity.

INTRODUCTION

As discussed in Part I of this paper, there has been considerable research interest in the environmentally-assisted cracking (EAC) response of low-alloy steels in elevated temperature aqueous environments. It has been recognized for several years that the tendency toward EAC increases with increasing sulfur content of the steels. This is because as a crack extends through a steel, it intersects metallurgical sulfide inclusions (e.g., MnS, FeS, etc.), and these dissolve upon contact with the hot water. EAC occurs when the concentration of sulfide (S^{2-}) or hydrosulfide (HS^-) ions at the crack tip reaches a critical concentration; probably about 5 ppm. Thus, in lieu of water-borne sulfide contaminants, the intersection of

---

* Fellow ASME

a growing crack with metallurgical sulfide inclusions constitutes the only process for supply of sulfides to the crack tip.

On the other hand, sulfide ions can be removed from the crack-tip region by any one, or more, of four mass-transport processes: 1) diffusion due to a concentration gradient, 2) ion migration due to a electrochemical potential (ECP) gradient, 3) fatigue "pumping" due to cyclic motion of the crack flanks, and 4) fluid flow induced within the crack cavity due to the presence of free stream fluid flow external to the crack. EAC initiates when the supply of sulfide ions to the crack tip exceeds the loss of sulfides through mass-transport for a sufficient period of time such that the critical crack-tip concentration is reached or exceeded. Hence, it is clear that any of the above processes that has a strong influence upon the competitive processes of sulfide supply and loss can play a possibly decisive role in the occurrence or non-occurrence of EAC.

Of the above four mass-transport processes, perhaps the most effective is the fourth: flow induced within the crack cavity by the action of an external free stream flow. Several studies have demonstrated the effectiveness of free stream flow in mitigating EAC, and these have been summarized by James et. al. (1995a, 1996a, 1996b). Several of the flow rate studies have utilized compact tension (CT) specimens, but two studies (James et al., 1995a, 1996b) employed surface-cracked specimens identical to those employed in Part I of this paper. It has been suggested (James et al., 1996b), however, that the mass-transport of sulfides from a CT specimen can be different than mass-transport from a tight semi-elliptical surface crack. Not only can sulfides be transported out along the sides of a crack in a CT specimen, but the crack-mouth opening displacement (CMOD) of a CT specimen is over twice that in a semi-elliptical surface crack of the same depth and loaded to the same level of the stress intensity factor, K. Therefore, in order to obtain a more prototypic mass-transport balance within the crack enclave, a surface-cracked specimen identical to that employed in Part I of this paper was utilized.

All of the studies on the effect of flow rate upon EAC, whether they employed CT specimens or surface-cracked specimens, have been conducted on specimens composed entirely of a low-alloy steel. However, some applications may involve a layer of corrosion resistant cladding that is overlaid on the steel. It has been suggested (Bramwell et al. 1995, Ruther et al. 1991) that the dissimilar metal couple involving the steel and the cladding could, in some cases, introduce galvanic effects not present in monolithic steel specimens, and hence influence the mass-transport kinetics of sulfide ions within the crack cavity. Therefore, the objective of this portion of the study on cladding effects was to characterize the effect of fluid flow upon the EAC response of relatively large semi-elliptical surface cracks penetrating a layer of cladding into a high-sulfur EAC-susceptible steel.

EXPERIMENTAL PROCEDURE

Materials

The low-alloy steel employed in this phase was a high-sulfur ASTM A302-B (UNS K12022) plate. Two specimens were tested, and were given the designations "SC-7" and "SC-8". The chemical composition is given in Table I. The tensile properties and strain-hardening characterization of this heat (Heat 21478-10) has been detailed by James (1995b). The size, shape, and area fraction of MnS inclusions play a role in EAC, and have been characterized by James and Poskie (1993) for this heat of steel. This heat of steel has also been employed in several EAC studies (James 1994a, 1995a, 1996b), and is being utilized in an on-going study of environmental effects upon fatigue initiation by Argonne National Laboratory (e.g., see Chung et al., 1995).

The cladding was applied to the A302-B plate employing a gas-metal-arc (GMA) process. Alloy EN82H (UNS N06082) filler metal was utilized. Following the weld-deposition process the cladding was machined to a uniform 6.35 mm depth. The cladding processes had introduced a strong residual magnetism in the low-alloy steel, and this was reduced by passing the weldments through degaussing coils. A piece of wrought Alloy 600 (UNS N06600) of sufficient size to allow the machining of the specimens was then joined to the Alloy EN82H by electron beam (EB) welding. The completed weldment assembly was then given a heat treatment at 607°C for 50 hours. The completed A302-B/Alloy EN82H/Alloy 600 specimen is illustrated in Figure 1.

Water Chemistry and Autoclave Conditions

Deaerated water containing 35-40 ml H_2/kg H_2O was employed in this study. Dissolved O_2 was therefore generally less than 10 ppb. The room temperature pH was about 10.2, while the calculated* pH at the test temperature of 243°C was 7.8. The room temperature conductivity was about 40 μS/cm. The electrochemical corrosion potential (ECP) of the specimen was measured during each test using a Ag/AgCl reference electrode. The relationship of Macdonald et al. (1979) was used to correct Ag/AgCl measurements to Standard Hydrogen Electrode (SHE) conditions. The autoclave volume was approximately 19 litres, and the water refreshment rate was approximately 50 ml/minute. Hence, on the average, about 6.3 hours would be required for one volume change of water; i.e., quasi-stagnant flow conditions.

The special apparatus that allowed active water flow along the crack is described in detail by James et al (1995a). Two active flow rates were employed in this study. The active flow applied to Specimen SC-7 was 26.8 litre/minute, resulting in an average free stream velocity of 1.69 m/sec. and a mean Reynolds Number (Re) of 224,000. The active flow applied to Specimen SC-8 was 75.0 litre/minute, resulting in an average free stream velocity of 4.74 m/sec. and Re = 625,000.

Specimen Design

Because of the important role that the mass-transport of sulfides plays in EAC susceptibility, a specimen employing a semi-elliptical surface crack was utilized in this study. This specimen, described in more detail by James and Wilson (1994a), features a tight "natural" intersection of the crack with the free surface. There are no notches nor crack-starter slits to "short circuit" the mass-transport of sulfide ions from the crack enclave. Hence, the mass-transport paths are more prototypic than in CT specimens. The K-solution of Newman and Raju (1984) was employed to analyze the results.

Relatively large cracks were employed in this study. Specimen SC-7 had an initial crack size at the start of testing of depth a = 14.05 mm and length 2c = 27.53 mm, while Specimen SC-8 had initial crack dimensions of a = 10.54 mm and 2c = 22.81 mm.

Testing Phases

No active measurements of crack extension were made during each test. Instead, differing stress ratios ($R = K_{min}/K_{max}$) were employed periodically to produce bands of different appearing texture on the fracture surface. These bands were used for post-test measurement of crack extension. At the completion of testing, the specimens were removed from the

*Calculated using MULTEQ (Electric Power Research Institute, Palo Alto, CA).

autoclave and then fractured following a soak in liquid nitrogen. Crack growth rates were then calculated using the "secant method" and employing post-test measurements from the fracture surface; $da/dN \approx \Delta a/\Delta N$ and $dc/dN \approx \Delta c/\Delta N$. The various test phases are given in Table II, and post-test photomacrographs of the fracture surfaces are shown in Figure 2.

The heat of high-sulfur A302-B that was used has exhibited EAC at the test temperature of 243°C in several previous studies (James et al., 1994a, 1995a, 1996b) employing unclad CT specimens and unclad surface-cracked specimens. In order to demonstrate that EAC will occur in a clad specimen, the initial test phase(s) in the present study were conducted under quasi-stagnant flow conditions; i.e., no active flow through the flow duct, and only the autoclave refreshment flow of 50 ml/minute through the general autoclave inventory.

RESULTS AND DISCUSSION

Electrochemical Results

The electrochemical corrosion potentials measured on Specimens SC-7 and SC-8 are shown in Figure 3. The reference electrode was positioned near the lower corner on the back side of each specimen, well away from the crack and the region of active fluid flow. The specimens were not electrically isolated from the autoclave and hence the ECP measurements represent specimen potentials and not necessarily free corrosion potentials.

The mean ECP measured for Specimen SC-7 over the duration of the test was -734 mV_{SHE}, and the mean ECP for Specimen SC-8 was -705 mV_{SHE}. These values agree well with similar measurements at 243°C in Part I of this paper, as well as with previous measurements by James (1994a) at 243°C.

It will be observed in Figure 3 that, when active fluid flow commenced on Specimen SC-7 at the start of Test Phase 2, a shift of approximately 56 mV toward more active (electronegative) potentials occurred over the course of Test Phase 2. This might imply an effect of fluid flow rate upon the ECP. Macdonald et al. (1993), studying austenitic stainless steels in high-oxygen water at 288°C, have observed the opposite trend: ECP values became more noble (electropositive) with increasing water flow rates. Because flow rate effects upon ECP are expected to be negligible under low-oxygen conditions (Macdonald et al. 1993), additional ECP measurements were made in conjunction with the testing of Specimen SC-8. In addition to the measurements of specimen potential on SC-8, free corrosion potential measurements were made on several insulated coupons of steel, platinum, and Alloy 600. Two of the insulated coupons, steel and Alloy 600, were located such that they were directly impinged upon by the discharge of the flow duct during high flow (4.74 m/sec.) testing. The results, given in Figure 4, show that the open-circuit potentials of all the specimens vary in a similar manner, and that there is very little difference in the OCP between materials. This result indicates that the OCP is controlled by the cathodic reaction and that galvanic effects upon the OCP between cladding and the underlying steel are negligible in low-oxygen water. Finally, although Specimen SC-8 was not electrically isolated from the loading train, the ECP for Specimen SC-8 is virtually identical to the free corrosion potential measured on the insulated steel coupon.

Crack Growth Results

Crack growth results for Specimens SC-7 and SC-8 are plotted in Figure 5 using the "time-domain" format first suggested by Shoji et al. (1981, 1983). In this format, the ordinate is the experimentally-observed value of da/dN divided by the load rise-time, t_r. The abscissa is the mean value of da/dN expected for a low-alloy steel of this type in an air environment at that

value of ΔK and R, again divided by t_r. In this case, the relationship developed by Eason et al. (1989) for A508-2 and A533-B steels in air was utilized. Also plotted in Figure 5 are the mean EAC and mean non-EAC curves developed by James (1994a) for a low-oxygen environment at 243°C using CT specimens.

Taking first the results for Specimen SC-7, it will be noted in Figure 5 that EAC was observed during the quasi-stagnant flow phase (Test Phase I). Following the quasi-stagnant phase, a flow of 1.69 m/sec. was established parallel to the crack and a static load equal to 75-percent of the maximum fatigue load was applied for a period of 289 hours (Test Phase 2). The purpose of the static-load test phase was to provide the opportunity for convective mass-transport with the crack at least partially open. An earlier study (James et al. 1995a) had shown that convective flow rate mitigation of EAC was not instantaneous upon the application of active flow, and that with average free stream velocity of 1.71 m/sec. for 288 hours adequately flushed the sulfides from a similarily-sized crack in an unclad high-sulfur A302-B surface-cracked specimen. No crack extension occurred during the static-load phase.

Following the 289-hour static-load active-flow period, fatigue cycling resumed on Specimen SC-7 at new values of cyclic frequency and R-ratio (Test Phase 3, see Table II) with the active flow of 1.69 m/sec. continuing. Test Phase 3 continued for 11528 cycles until excessive displacement occurred due to extensive crack extension (see Figure 2). That the crack extension observed during Test Phase 3 was greater than expected (even under mean EAC conditions) can be seen in Figure 6. Figure 6 compares the experimentally observed crack dimensions with the predicted behavior. The details of the prediction methodology are given in Part I of this paper. The predictions are based on either mean non-EAC behavior, or mean EAC behavior (see the dotted lines in Figure 5) in the A302-B steel at the point of deepest crack penetration (Point "A"), and on the mean crack growth behavior given by James and Mills (1995c) for Alloy EN82H in a low-oxygen water environment at 243°C for the crack tips at the surface (Points "C"). Crack extension at Point(s) "C" was calculated to be very small ($\approx$0.11 mm) during Test Phase I, and indeed little or no crack extension was observed on the surface for this phase. James and Mills (1995c) have shown that at R = 0.7, the crack growth relation is bilinear changing to a steeper slope, and very low crack growth rates ($\approx 5.65 \times 10^{-6}$ mm/cycle) would be expected at the mean ΔK = 9.4 MPa$\sqrt{m}$ at Point "C" for Test Phase I. It is clear, however, from both Figures 5 and 6 that EAC was not only observed at Point "A", but the associated crack growth rate was actually somewhat higher than the mean EAC rate. It is also clear when comparing the actual and predicted values of the crack depth, a, at the completion of testing that EAC was also observed at Point "A" during Test Phase 3. This is in spite of the imposition of a mean free stream velocity of 1.69 m/sec. parallel to the crack for 384 hours during Test Phase 3 as well as for 289 hours during Test Phase 2 prior to the start of fatigue cycling. The finite width correction term in surface-crack K-solutions of Newman and Raju (1984) becomes increasingly inaccurate as the crack length (2c) approaches the specimen width (W = 50.8 mm). Hence, the predictions for Test Phase 3 in Figure 6 are not considered highly accurate. Nevertheless, it is clear that a free stream velocity of 1.69 m/sec. did not mitigate EAC in this clad specimen. It should be noted that the same flow velocity did turn off EAC in a surface crack of similar size in an unclad specimen of the same heat of steel (James et al., 1995a, 1996b).

Because of the lack of flow rate benefit observed on Specimen SC-7, Specimen SC-8 was tested using a mean free stream velocity of 4.74 m/sec. In addition, the static-load flow period (Test Phase "3" for Specimen SC-8) was increased to 512 hours. Again, no cycling and crack extension occurred during the static-load phase. In order to provide additional information, two quasi-stagnant flow test phases (at R = 0.7 and R = 0.1) and two active flow test phases (at R = 0.7 and R = 0.1) were utilized (see Table II). As noted in Figure 5, EAC

was observed in both Test Phases 1 and 2 under quasi-stagnant flow conditions, and the observed crack growth rates are close to the mean EAC line established by James (1994a) using CT specimens. However, Test Phase 4, which followed the 512-hour static-load flow phase, also exhibited EAC in spite of the relatively high flow velocity. This may be seen both in the time-domain plot of Figure 5 and the crack extension predictions of Figure 7. However, the prediction of Figure 7 suggests that at least toward the end of Test Phase 5, the active flow had become at least partially effective in mitigating EAC. This is because although the post-test crack depth was greater than that predicted for mean non-EAC conditions, it is significantly less than that predicted for mean EAC conditions. 845 hours of active flow at a mean velocity of 4.74 m/sec. had transpired at the start of Test Phase 5, and 2203 total hours of high flow had passed by the end of Test Phase 5. Figure 5 shows that somewhat less than a "mean case" of EAC occurred during Test Phase 4. It is therefore likely that a somewhat less severe case of EAC was operative at the start of Test Phase 5, and as Test Phase 5 progressed (a duration of 1358 hours) the continuing active flow slowly reduced the inventory of sulfide ions at the crack tip thereby reducing crack growth rates. It may even be speculated that toward the end of Test Phase 5, crack growth rates may have approached the non-EAC level. This will be discussed more in a later section on computational fluid dynamics (CFD) modeling. It should be noted that both Test Phases 4 and 5 occurred in a time-domain regime where EAC can, and does, occur. James (1994a) has shown that EAC is persistent in these high-sulfur steels in this time-domain regime. Hence, any diminution of EAC can be attributed to flow rate effects.

James et al. (1995a, 1996b) tested an unclad surface-cracked specimen of the same high-sulfur A302-B steel with approximately the same crack size at a very similar flow rate (about 5.0 m/sec.). Complete mitigation of EAC was observed with crack growth rates approximately equal to the mean air line. The only difference between the two experiments is, of course, the presence of cladding on Specimen SC-8. The photomicrographs of Figure 2 (as well as those in Figure 3 in Part I of this paper) reveal that crack surface in the clad portion of the fracture surfaces has a much "rougher" appearance. James and Mills (1995c) studied the fatigue crack propagation behavior of weld-deposited Alloy EN82H in a low-oxygen water environment at 243°C. They observed that the mode of crack extension was trans-dendritic, and that the cracks often propagated "up" along a single crystallographic plane all way the across a relatively large dendrite, and when the dendrite boundary was reached growth might continue "down" along a single plane in the adjacent dendrite. This sort of "sawtooth" trans-dendritic growth is evident in the photomacrographs of Figure 2 as well as in Figure 3 of Part 1 of this paper.

In order to quantify the surface roughness, extensive profilometry measurements were made in the crack enclave of a surface-cracked specimen of A302-B steel (Specimen SC-10 reported by James et al., 1995a). The profilometer* employed a 2.5 μm diameter stylus to characterize the statistics associated with the roughness of the crack surface. The arithmetic average roughness was 2.6 μm, and the root-mean-square roughness corresponding to the arithmetic average roughness was 3.2 μm. The same profilometer could not be employed in the cracked region of the cladding because of possible damage to the stylus due to the extreme roughness. However, optical measurements of height differences between adjacent "peaks" and "valleys" in the crack surface in the cladding revealed many in the 200-380 μm range, and a few were in the 760-840 μm range. Although the roughness measurements in the steel and the cladding are not directly comparable, it is clear that there may be approximately two orders of magnitude difference between the crack surface roughness in the steel and that in the cladding. It is believed that the greater crack surface roughness in

*Dektak 8000 (Sloan Technology Division of Veeco Corp.)

the cladding acts as an impediment in the exchange of water between the free stream and the steel portion of the crack enclave.

Crack-Opening Displacements

As a prerequisite to the computational fluid dynamics (CFD) calculations to be discussed later, it is necessary to calculate the crack-opening displacements expected for Specimen SC-8. Specimen SC-8 had dimensions of a $\approx$14.2 mm and 2c $\approx$ 25.5 mm at the start of the Test Phase 4 (cyclic load active fluid flow phase). The elastic crack tip opening displacement (CTOD or δ_e) can be approximated by

$$\delta_e = \frac{K^2}{m\sigma_y E} \qquad \text{Eq. [1]}$$

where K = the stress intensity factor, "m" is a constraint factor, σ_y is the yield strength, and E=Young's Modulus. "m" generally ranges between 1 and 2, and m $\rightarrow$ 2 for high constraint and/or high strain-hardening while m $\rightarrow$ 1 for low constraint and/or low strain hardening. Because both A302-B (James, 1995b) and EN82H exhibit relatively high strain-hardening, and because the elastic "T-stresses" (a measure of constraint) are relatively high for most positions along a semi-elliptical crack front except Point(s) "C" (Nakamura & Parks, 1992, and Wang & Parks, 1992), "m" was chosen equal to 2 for the present case. σ_y was taken to be 310 MPa and 241 MPa for A302-B and EN82H, respectively, at 243°C. E was taken to be 191 GPa and 193 GPa for A302-B and EN82H, respectively, at 243°C. Using the above values of CTOD were calculated for Specimen SC-8: $\delta_e = 4.57 \times 10^{-3}$ mm for A302-B steel at Point "A", and $\delta_e = 1.20 \times 10^{-2}$ mm for EN82H at Point(s) "C". Although the specimens are generally elastically loaded, some limited plasticity nevertheless exists at the crack tip. Reuter and Lloyd (1990) have measured actual total CTOD values for surface cracks in steel specimens, and for the specimens with the lowest stress levels ($\sigma_{max} \approx \sigma_y$) found that

$$\delta_{total} \approx 2.33\ \delta_e \qquad \text{Eq. [2]}$$

Therefore, Equation [2] was applied to the previously calculated values of δ_e to produce: $\delta_{total} = 1.06 \times 10^{-2}$ mm for the point of deepest penetration, (Point "A") and $\delta_{total} = 2.79 \times 10^{-2}$ mm for the two surface crack tips (Point "C"). Crack mouth opening displacements (CMOD) at the free surface were calculated using the relationships of Raju et al. (1992) producing: CMOD = 2.59×10^{-2} mm at the maximum test stress. The maximum crack opening at the free surface occurs in the center of the crack, and is equal to δ_{total} + CMOD. These calculations are illustrated schematically in Figure 8.

It is clear from Figure 8 that the calculated crack openings for Specimen SC-8 at the start of Test Phase 4 are small, even allowing for some limited crack-tip plasticity. These calculations are, of course, dependent upon the assumptions made in the calculations (particularly "m" and δ_{total}/δ_e), but reasonable variations in these assumptions are not expected to produce dramatic changes in the final answer.

CFD Model

To assist in the understanding of the experimental observations of flow rate effects, each of the experiments was analyzed employing the finite element CFD code FIDAP.* FIDAP has been employed previously to study convective mass-transport within pits and cavities, e.g., see Alkire et al. (1984, 1990) and Harb et al. (1988, 1989). Dr. M. Psaila-Dombrowski, presently at the Babcock & Wilcox Research Center, performed some unpublished CFD analyses of flow effects on surface cracks during a post-doctoral assignment at the General Electric R&D Center. However, with the exception of the recent paper by James et al. (1996b), CFD has not been employed to study mass transport within tight semi-elliptical cracks in the manner to be described herein.

The CFD models used in the analysis of relevant flow fields in a surface-cracked EAC test specimen with weld-deposited Alloy EN82H cladding simulate a single-phase, isothermal, incompressible, turbulent/laminar flow in a two-dimensional (2-D) flow field. The CFD models of the EAC test specimens explicitly account for the crack enclave, the planar surface surrounding the crack opening, and the free stream flow parallel to the crack opening. In the 2D models, 38.1 mm of planar surface upstream and downstream of the crack opening is included for free stream flow development and recovery, respectively. The modelled crack geometry had dimensions as shown in Figure 8. The variable crack width (crack opening) as shown in Figure 8 was accounted for in the model and the clad depth of 6.35 mm was assumed. Dirchlet boundary condition, including a flat velocity profile, is specified at the inlet and a zero traction (zero stress) boundary condition is specified at the outlet. The free stream flow velocity was assumed to be parallel to the surface crack and a free stream velocity of 4.74 m/sec was assessed. The computational mesh employed was similar to that described earlier (James et. al, 1996b), with additional mesh refinement in the region representing the cladding. A detailed description of the CFD modelling techniques, analysis procedures, and parameter sensitivity studies utilized in the analysis was described by James et. al, 1996b.

In the current 2-D analysis, a volumetric body force acting on the fluid is applied to the momentum equation as an additional source term (momentum sink) to simulate the effects of wall friction. The revised momentum equation used in the 2-D CFD calculations is:

$$\rho\left(\frac{\partial u_i}{\partial t} + u_j u_{i,j}\right) = \sigma_{ij,j} + \rho f_i \qquad \text{Eq. [3]}$$

where ρ is density, σ_{ij} is the stress tensor and f_i is the body force per unit mass. In 2-D CFD analysis of flow fields within the crack enclave of the EAC test specimens, since the analysis only considers flow-forced, single-phase, turbulent/laminar flow under isothermal conditions, the only body force term present in the momentum equation is the one specified to simulate wall friction. The body force term used to simulate wall friction is the frictional force correlation for laminar flow between parallel plates,

$$f = \frac{-12\mu U}{\rho S^2} \qquad \text{Eq. [4]}$$

* FIDAP, Fluid Dynamics International, Evanston, IL.

where f is the frictional force, μ is the viscosity, U is the velocity, ρ is the density, and S is the distance between the plates. For a given calculation, the volumetric body force simulating the wall friction is calculated for every element in the crack enclave flow field. The local crack width (S) is calculated for every element in the crack enclave using B-spline polynomial fits of the crack enclave surfaces. Thus, the 3D geometry of the crack enclave is accounted for in the analysis even though the actual calculation is being performed in 2D. In the current analysis of EAC test specimens with a surface crack penetrating EN82H cladding into a high-sulfur steel, a different formulation of volumetric body force is used to simulate the additional viscous losses due to the greater crack surface roughness of the clad. In this formulation, the volumetric body force is modelled as

$$\rho f_i = \frac{2.0\tau_w}{S} \qquad \text{Eq. [5]}$$

where τ_w is the wall shear stress and S is the channel spacing or thickness. A simple force balance shows that the fluid shear stress τ (shear force/unit surface area) imposed on the wall of a uniform duct by the friction of the flowing fluid is proportional to the friction factor:

$$\tau = \frac{\rho U^2}{2}\left(\frac{f_f}{4}\right) \qquad \text{Eq. [6]}$$

where U is fluid velocity and f_f is the friction factor. Thus, it follows that the body force for unit mass is

$$\rho f_i = \frac{-\rho f_f U^2}{4S} \qquad \text{Eq. [7]}$$

The actual implementation of this body force in FIDAP is

$$\rho f_i = \frac{-\rho f_f |U| U_i}{4S} \qquad \text{Eq. [8]}$$

This implementation allows for the body force term to be applied to each directional component of the momentum equation. Since the friction factor is explicitly a part of the body force term, the friction factor can be varied in a sensitivity study to identify a particular body force formulation which most appropriately simulates the additional viscous losses due to the greater crack surface roughness of the EN82H clad. Based on such a sensitivity study, judgement was employed to select a friction factor that accounted for the relative physical dimensions of the crack surface roughness in the cladding and in the steel.

CFD Analysis Results for Specimen SC-8

A CFD analysis was performed to characterize the relevant flow fields in surface-cracked EAC test specimens with weld-deposited Alloy EN82H cladding. In particular, this analysis assessed the effects that macroscopically-rough fracture surface of the EN82H clad have on the crack enclave flow field and on the dynamics of the interaction between the crack enclave and free stream flow fields. The analysis results showed that the added resistance to flow

brought on by the macroscopically-rough fracture surface of the EN82H cladding can act as a significant impediment to interchange of fluid between the crack enclave and the free stream. As a result, the CFD analysis provided a plausible explanation as to why active free stream flows failed to mitigate EAC as rapidly in the EN82H-clad EAC test specimens.

The CFD analysis results for the SC-8 EAC test specimen show that even at a relatively high active free stream flow velocity of 4.74 m/sec., the interaction between the free stream and crack enclave flow fields is severely limited by the added resistance to flow brought on by the macroscopically-rough fracture surface of the EN82H cladding. Figure 9 presents the predicted interaction pattern between the free stream and crack enclave flow fields as depicted by the Y-component of velocity (UY) along the free stream - crack opening interface. In Figure 9, a negative UY velocity indicates flow into the crack enclave and a positive UY velocity indicates flow out of the crack enclave. As can be seen in Figure 9, although the flow appears to enter the crack near the leading edge of the crack and exit towards the trailing edge of the crack, significant amount of flow appears to be entering and exiting the crack enclave in the middle region of the crack opening. This type of interface flow pattern indicates that the free stream flow is not penetrating very deep into the crack enclave and a stable flow pattern in the crack enclave capable of evenly "flushing" the crack tip is not likely to be established. Given the aforementioned interaction pattern, it is likely that the most effective mitigation of EAC by the flow would be limited to the leading edge crack tip region and, as a result, the shape of the EAC crack extension is not likely to be symmetric. This was indeed the observed result for Specimen SC-8 (see Figure 2).

Figure 10 presents calculated streamline contour plot of the flow field within the EN82H cladded crack enclave of the SC-8 EAC test specimen. The detailed streamline contour plot of the crack enclave flow field is displayed by setting the minimum and maximum stream functions to be plotted to those values representative of the crack enclave flow field. As can be seen from Figure 10, the interaction between the free stream and crack enclave flow fields is largely limited to the cladded region. Some of the free stream flow, however, does penetrate beyond the cladded region and, in turn, induces a weak half-loop flow pattern in the uncladded region of the crack enclave. It can be also seen from Figure 10, the induced flow field in the uncladded region of the crack enclave is largely limited to the region adjacent to the cladding/base metal interface. Moreover, a discernable, stable secondary flow pattern is not established near the crack tip region. Figure 11 presents the predicted velocity magnitude (speed) profile of the flow in the crack enclave and adjoining free stream along a line traversing from the bottom of the crack tip to the top of the adjoining free stream. Due to the large disparity in magnitude of free stream velocity to crack enclave velocity (several orders of magnitude), the speed profile is plotted in logarithmic scale. As can be seen from Figure 11, the flow speed profile has three distinct features representative of the flow fields in the free stream, cladded, and uncladded regions of the crack enclave. The key transition points displayed in the speed profile is the sharp drop-off in fluid speed in going from free stream to the cladded region of the crack enclave and a concomitant drop-off in fluid speed in going from the uncladded region of the crack enclave to the cladded region of the crack enclave. Thus, the shape of the fluid speed profile indicates that the crack surface roughness of the EN82H cladding impedes the flow into and out of the crack enclave. The fluid speed profile in Figure 11 also shows the sharp, non-linear drop-off in fluid speed as the crack tip is approached. The CFD model predicts a crack tip flow velocity on the order of 1.3×10^{-4} m/sec. An earlier CFD analysis on a crack of similar size penetrating into steel only (i.e., no cladding) and subjected to a free-stream flow of similar magnitude, produced a calculated crack-tip velocity approximately 20 times the above calculation for Specimen SC-8 (James et. al, 1996b). This provides another illustration of the effect of cladding upon convective mass-transport.

The CFD analysis results indicate that the macroscopically-rough crack surface of the EN82H clad may not only provide a significant impediment to the free stream flow entering the crack, but also to the flow exiting the crack enclave. Thus, the macroscopic-rough crack surface of the EN82H cladding may seriously inhibit the interaction between the free stream and crack enclave flow fields and, as a result, a stable, convective flow pattern capable of "sweeping" the crack tip is not established in the crack enclave to the same degree as in unclad cracks. It appears that even at high free stream flow conditions (4.74 m/sec.) the greater crack surface roughness of the EN82H cladding impedes the mass transport of sulfide ions from the crack tip to the free stream and, as such, EAC is not as effectively mitigated.

CONCLUSION

Corrosion-fatigue crack propagation experiments were conducted employing relatively large, tight semi-elliptical surface cracks penetrating approximately 6.35 mm of weld-deposited cladding into a high-sulfur EAC-susceptible steel. A free stream flow of 1.69 m/sec. directed parallel to the crack did not mitigate EAC. A free stream velocity of 4.74 m/sec. may have largely mitigated EAC toward the end of the active flow test phases ($\approx$2200 hours), but any EAC mitigation was far less dramatic than earlier results on similar cracks in an unclad specimen subjected to approximately the same flow velocity. CFD modelling that accounted for the demonstrably greater crack surface roughness in the cladding confirmed that the cladding was an impediment to interaction between the free stream and the crack tip region, thereby hindering the mass-transport of sulfide ions from the crack tip region.

ACKNOWLEDGEMENTS

This work was performed under a U. S. Department of Energy contract with the Bettis Atomic Power Laboratory, a unit of the Westinghouse Electric Corporation. The experimental work was conducted under a subcontract with Materials Engineering Associates of Lanham, MD. T. F. Anater of Bettis performed the profilometric measurements of crack surface roughness. Dr. W. C. Moshier of Bettis provided valuable suggestions on the interpretation of the electrochemical results. Dr. M. J. Psaila-Dombrowski of Babcock & Wilcox provided the drawing of the grid employed in Figure 8.

REFERENCES

Alkire, R. C., Reiser, D. B., and Sani, R. L., 1984, "Effect of Fluid Flow on Removal of Dissolution Products from Small Cavities," *Journal of the Electrochemical Society*, Vol. 131, No. 12, pp. 2795-2800

Alkire, R. C., Deligianni, H., and Ju, J-B., 1990, "Effect of Fluid Flow on Convective Transport in Small Cavities," *Journal of the Electrochemical Society*, Vol. 137, No. 3, pp. 818-824

Bramwell, I. L., Tice, D. R., Worswick, D., and Heys, G. B., 1995, "The Effect of Stainless Steel Overlay Cladding on Corrosion Fatigue Crack Propagation in a Pressure Vessel Steel in PWR Primary Coolant", *Proceedings Seventh International Symposium on Environmental Degradation of Materials in Nuclear Power Systems - Water Reactors,* Vol. 2, NACE, 1995, pp. 1157-1168

Chung, H. M., Chopra, O. K., Erck, R. A., Kassner, T. F., Michand, W. F., Ruther, W. E., Sanecki, J. E., Shack, W. J., and Soppet, W. K., 1995, "Environmentally Assisted Cracking in Light Water Reactors," NUREG/CR-4667, Vol. 18

Eason, E. D., Andrew, S. P., Warmbrodt, S. B., Nelson, E. E., and Gilman, J. D., 1989, "Analysis of Pressure Vessel Steel Fatigue Tests in Air," *Nuclear Engineering and Design*, Vol. 115, No. 1, pp. 23-30

Harb, J. N., and Alkire, R. C., 1988, "A Finite Element Model for the Dissolution of Corrosion Pits in the Presence of Fluid Flow," *International Journal for Numerical Methods in Fluids*, Vol. 8, No. 12, pp. 1513-1522

Harb, J. N., and Alkire, R. C., 1989, "The Effect of Fluid Flow on Growth of Single Corrosion Pits," *Corrosion Science*, Vol. 29, No. 1, pp. 31-43

James, L. A. and Poskie, T. J., 1993, "Correlation Between MnS Area Fraction and EAC Behavior," WAPD-T-3012, available from US DOE Office of Scientific Technical Information, P.O. Box 62, Oak Ridge, TN 37831

James, L. A., 1994a, "The Effect of Temperature and Cyclic Frequency Upon Fatigue Crack Growth Behavior of Several Steels in an Elevated Temperature Aqueous Environment," *Journal of Pressure Vessel Technology*, Vol. 116, No. 2, pp. 122-127

James, L. A., and Wilson, W. K., 1994b, "Development of a Surface-Cracked Specimen," *Theoretical and Applied Fracture Mechanics*, Vol. 20, No. 2, pp. 115-121

James, L. A., Wire, G. L., and Cullen, W. H., 1995a, "The Effect of Water Flow Rate Upon the Environmentally-Assisted Cracking Response of a Low-Alloy Steel," *Journal of Pressure Vessel Technology*, Vol. 117, No. 3, pp. 238-244

James, L. A., 1995b, "Ramberg-Osgood Strain-Hardening Characterization of an ASTM A302-B Steel," *Journal of Pressure Vessel Technology*, Vol. 117, No. 4, pp. 341-345

James, L. A., and Mills, W. J., 1995c, "Fatigue Crack Propagation Behavior of Wrought Alloy 600 and Weld-Deposited EN82H in an Elevated Temperature Aqueous Environment", *Service Experience, Structural Integrity, Severe Accidents, and Erosion in Nuclear and Fossil Plants,* ASME Publication PVP-Vol. 303, pp. 21-36

James, L. A., and Van Der Sluys, W. A., 1996a, "The Effect of Aqueous Environments Upon the Initiation and Propagation of Fatigue Cracks in Low-Alloy Steels," *Proceedings of Corrosion 96 Research Topical Symposia*, NACE, 1996, pp. 176-209

James, L. A., Lee, H. B., and Wire, G. L., 1996b, "The Effect of Water Flow Rate Upon the Environmentally-Assisted Cracking Response of a Low-Alloy Steel: Experimental Results Plus Modeling," *Journal of Pressure Vessel Technology*, in press (WAPD-T-3067)

Macdonald, D. D., Scott, A. C., and Wentrcek, P., 1979, "Silver-Silver Chloride Thermocells and Thermal Liquid Junction Potentials for Potassium Chloride Solutions at Elevated Temperatures," *Journal of the Electrochemical Society*, Vol. 126, No. 9, pp. 1616-1624

Macdonald, D. D., Song, H., Makela, K., and Yoshida, K., 1993, "Corrosion Potential Measurements on Type 304 SS and Alloy 182 in Simulated BWR Environments," *Corrosion*, Vol. 49, No. 1, pp. 8-16

Nakamura, T. and Parks, D. M., 1992, "Determination of Elastic T-Stress Along Three-Dimensional Crack Fronts Using an Interaction Integral," *International Journal of Solids and Structures*, Vol. 29, No. 13, pp. 1597-1611

Newman, J. C. And Raju, I. S., 1984, "Stress Intensity Factor Equations for Cracks in Three-Dimensional Finite Bodies Subjected to Tension and Bending Loads", NASA Technical Memorandum 85793

Raju, I. S., Newman, J. C., and Atluri, S. N., 1992, "Crack-Mouth Displacements for Semielliptical Surface Cracks Subjected to Remote Tension and Bending Loads," *Fracture Mechanics: Twenty-Second Symposium (Volume II)*, ASTM STP 1131, pp. 19-28

Reuter, W. G., and Lloyd, W. R., 1990, "Measurements of CTOD and CTOA Around Surface-Crack Perimeters and Relationships Between Elastic and Elastic-Plastic CTOD Values," *Surface Crack Growth: Models, Experiments, and Structures*, ASTM STP 1060, pp. 152-176

Ruther, W. E., Shack, W. J., Chung, H. M., Kassner, T. F., and Soppet, W. K., 1991, "Environmentally Assisted Cracking in Light Water Reactors", NUREG/CR-4667, Vol. 10

Shoji, T., Takahashi, H., Suzuki, M., and Kondo, T., 1981, "A New Parameter for Characterizing Corrosion Fatigue Crack Growth," *Journal of Engineering Materials and Technology*, Vol. 103, No. 4, pp. 298-304

Shoji, T., Takahaski, H., Nakajima, H., and Kondo, T., 1983, "Role of Loading Variables in Environment Enhanced Crack Growth for Water-Cooled Nuclear Reactor Pressure Vessel Steels," NUREG/CP-0044, Vol. 2, pp. 143-171

Wang, Y. Y. and Parks, D. M., 1992, "Evaluation of the Elastic T-Stress in Surface-Cracked Plates using the Line-Spring Method," *International Journal of Fracture*, Vol. 56, No. 1, pp. 25-40

Table I

CHEMICAL COMPOSITIONS

Alloy	Heat No.	C	Mn	P	S	Si	Mo	Cu	Ni	Cr	Fe	Ti	Cb+Ta
A302-B	21478-10	0.19	1.17	0.015	0.027	0.21	0.48	-	-	-	Bal.	-	-
A302-B	21478-10	0.19	1.29	0.026	0.024	0.22	0.55	-	-	-	Bal.	-	-
A302-B	21478-10	0.21	1.34	0.021	0.027	0.22	0.51	0.22	0.23	0.14	Bal.	-	-
A302-B	21478-10	-	1.21	-	0.024	0.21	0.48	0.22	0.21	0.14	Bal.	-	-
EN82H (GMA)	NX4644DK	0.04	2.99	0.001	0.001	0.06	-	0.02	72.74*	19.81	1.38	0.43	2.53

*Ni+Co

TABLE II

SUMMARY OF TEST PHASES

	Specimen SC-7			Specimen SC-8				
	Phase 1	Phase 2	Phase 3	Phase 1	Phase 2	Phase 3	Phase 4	Phase 5
Flow Rate (m/sec.)	Q.S.	1.69	1.69	Q.S.	Q.S.	4.74	4.74	4.74
Fatigue Cycles	10000	N/A	11528	10003	800	N/A	20000	19951
Time (hours)	167	289	384	161	79	512	333	1358
Stress Ratio*	0.7	N/A	0.1	0.7	0.1	N/A	0.7	0.1
Frequency (Hz)	1.67E-2	Static**	8.33E-3	1.67E-2	2.80E-3	Static**	1.67E-2	4.08E-3

Q.S. = Quasi-stagnant

*Maximum fatigue load = 133.4 kN for all active cycling phases on both specimens.
**Static Load = 75% of maximum fatigue load = 100 kN

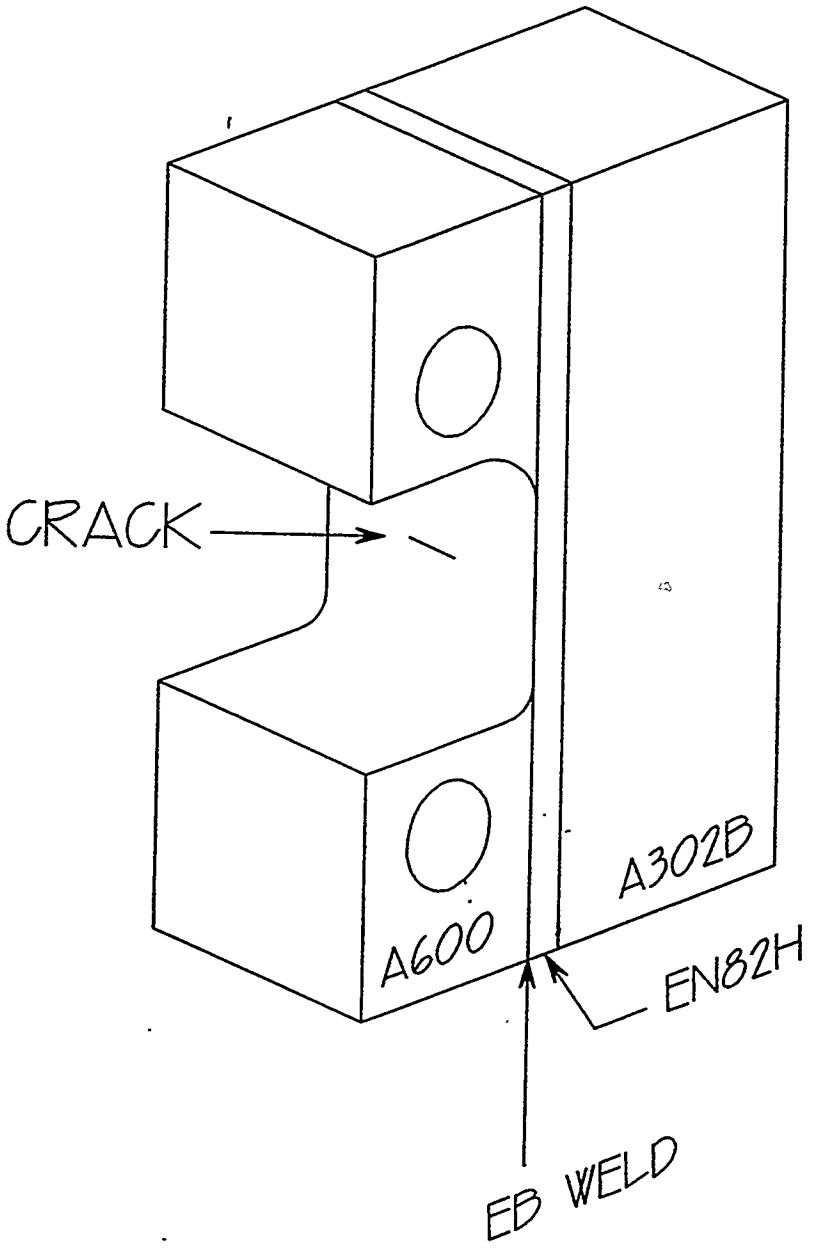

Figure 1 Schematic of the composite A302-B/EN82H/Alloy 600 specimen with the precracking web removed. See Figure 1 of Part I for the specimen with the precracking web in place.

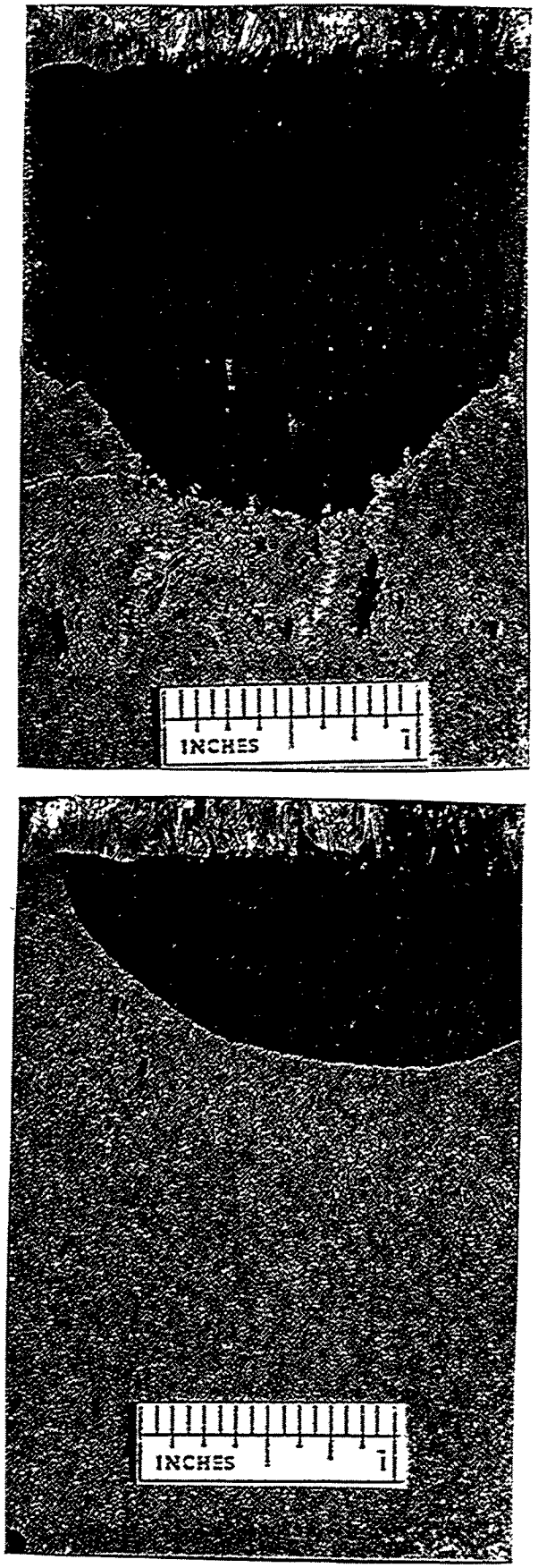

Figure 2 Post-test photomacrographs of the fracture faces of Specimen SC-7 (top) and SC-8 (bottom). The direction of flow was left to right in both cases.

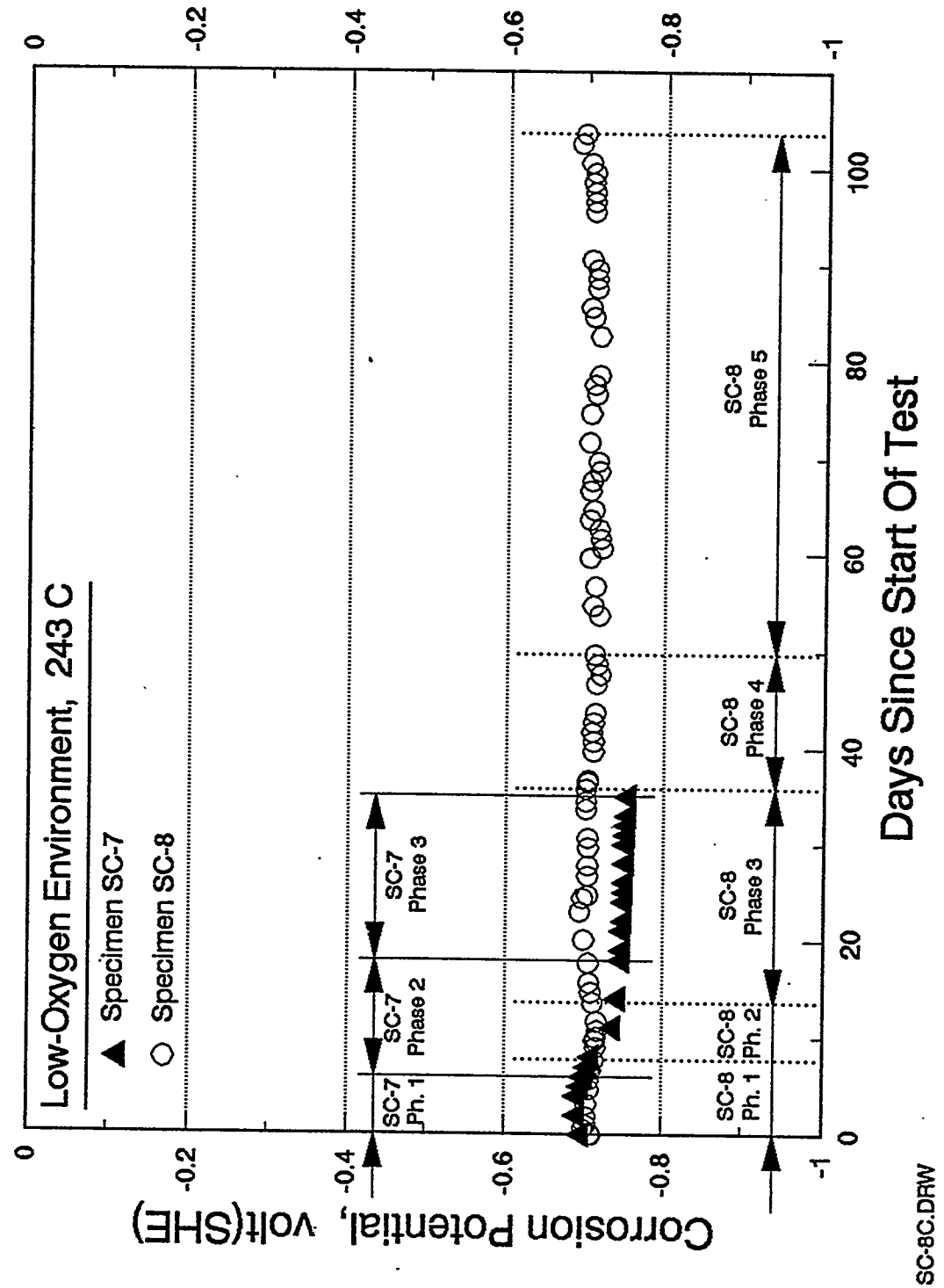

Figure 3 Electrochemical corrosion potentials for Specimens SC-7 and SC-8

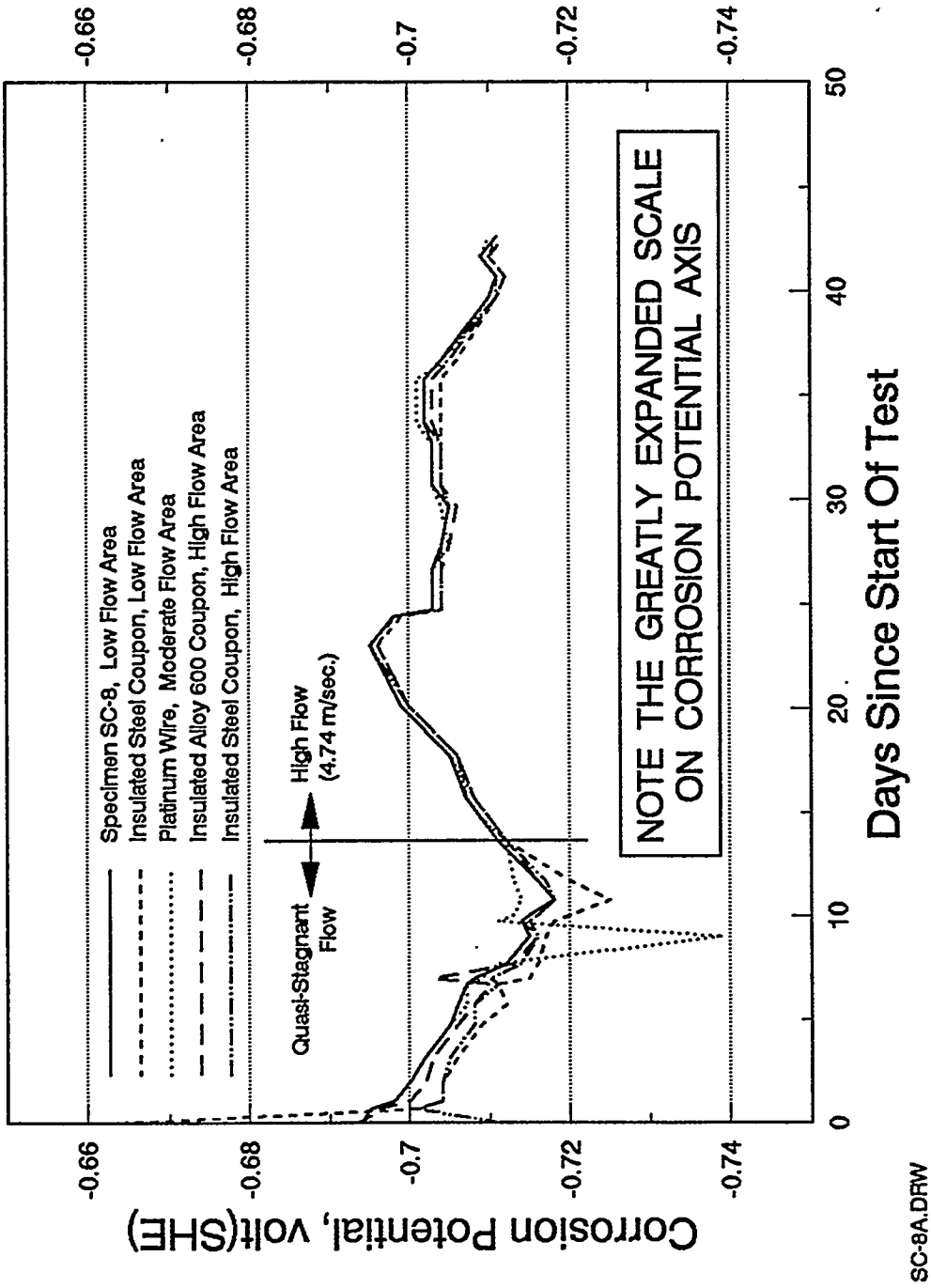

Figure 4 The effect of flow rate upon the corrosion potentials of several materials during the early stages of the experiment on Specimen SC-8.

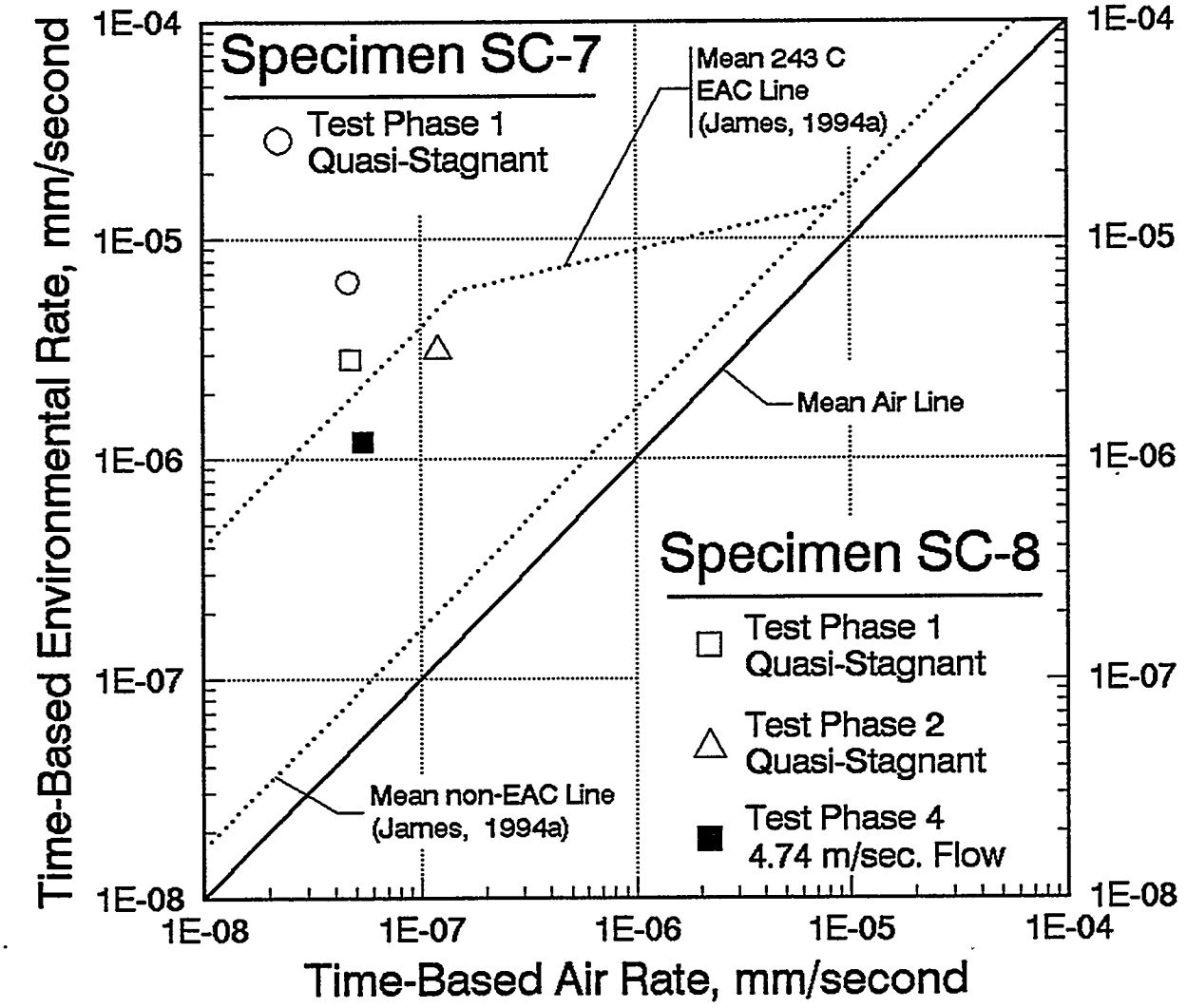

SC-8C.DRW

Figure 5 Time-domain plot of the fatigue crack growth behavior observed at the point of deepest penetration (Point "A") on clad surface-cracked Specimens SC-7 and SC-8.

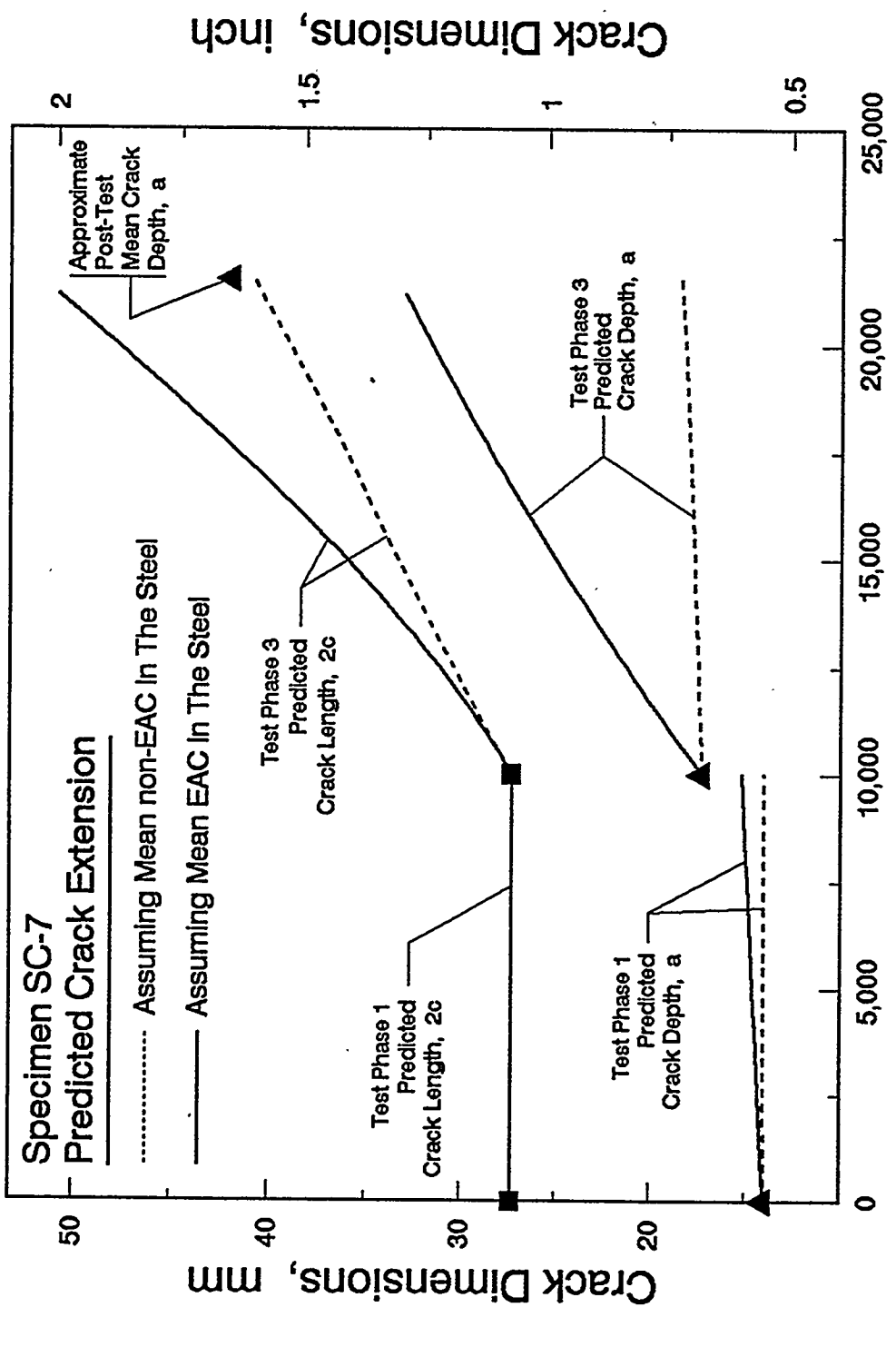

Figure 6 Comparison of predicted (lines) and observed (data symbols) crack dimensions for the two cyclic fatigue test phases on Specimen SC-7. It should be noted that these predictions become increasingly inaccurate as the crack length (2c) approaches the specimen width (W=50.8 mm).

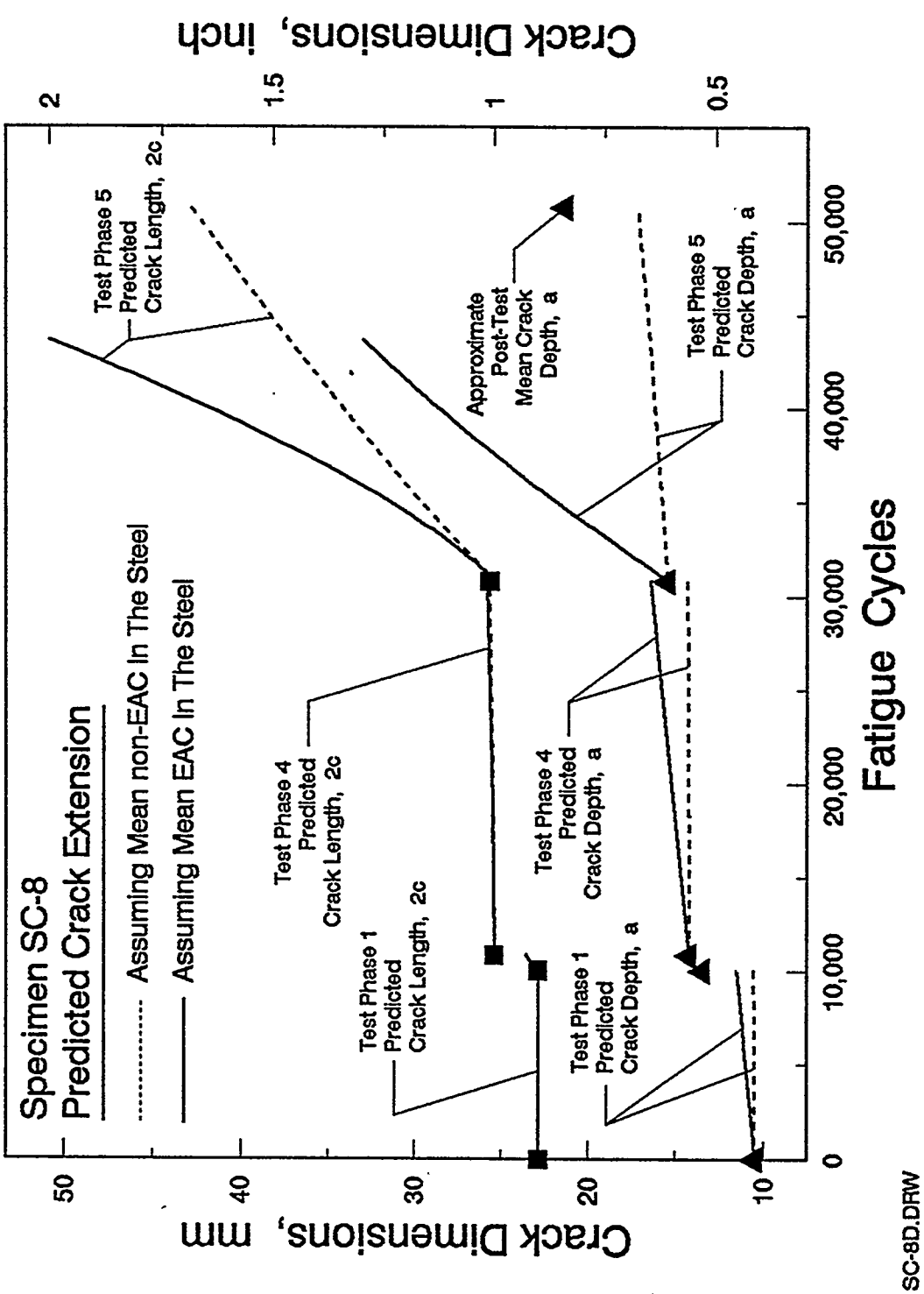

Figure 7 Comparison of predicted (lines) and observed (data symbols) crack dimensions for the four cyclic fatigue test phases on Specimen SC-8. It should be noted that these predictions become increasingly inaccurate as the crack length (2c) approaches the specimen width (W=50.8 mm).

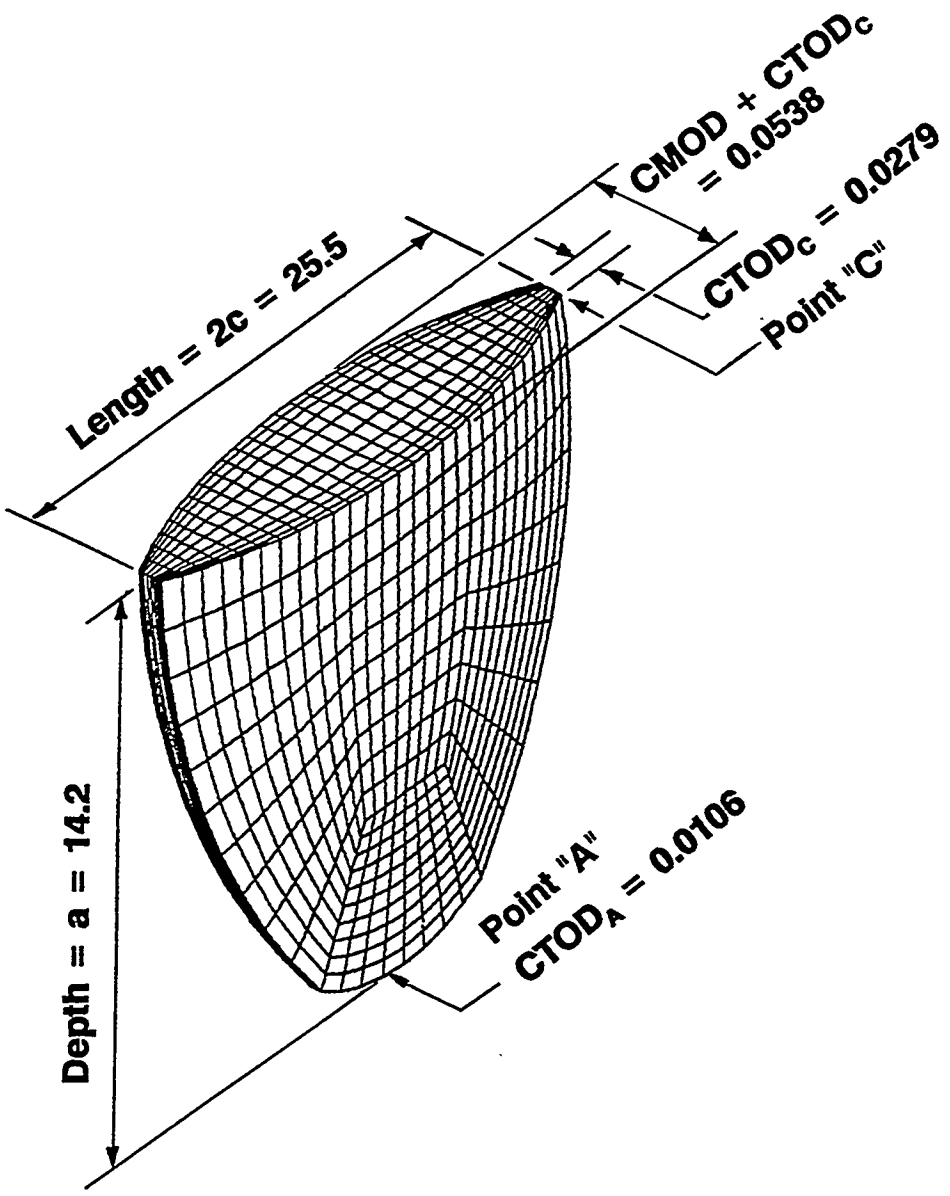

Figure 8 Calculated CTOD and CMOD values for Specimen SC-8 at the start of Test Phase 4 (active flow cyclic-load phase). Scales are distorted for clarity of viewing. All dimensions in mm.

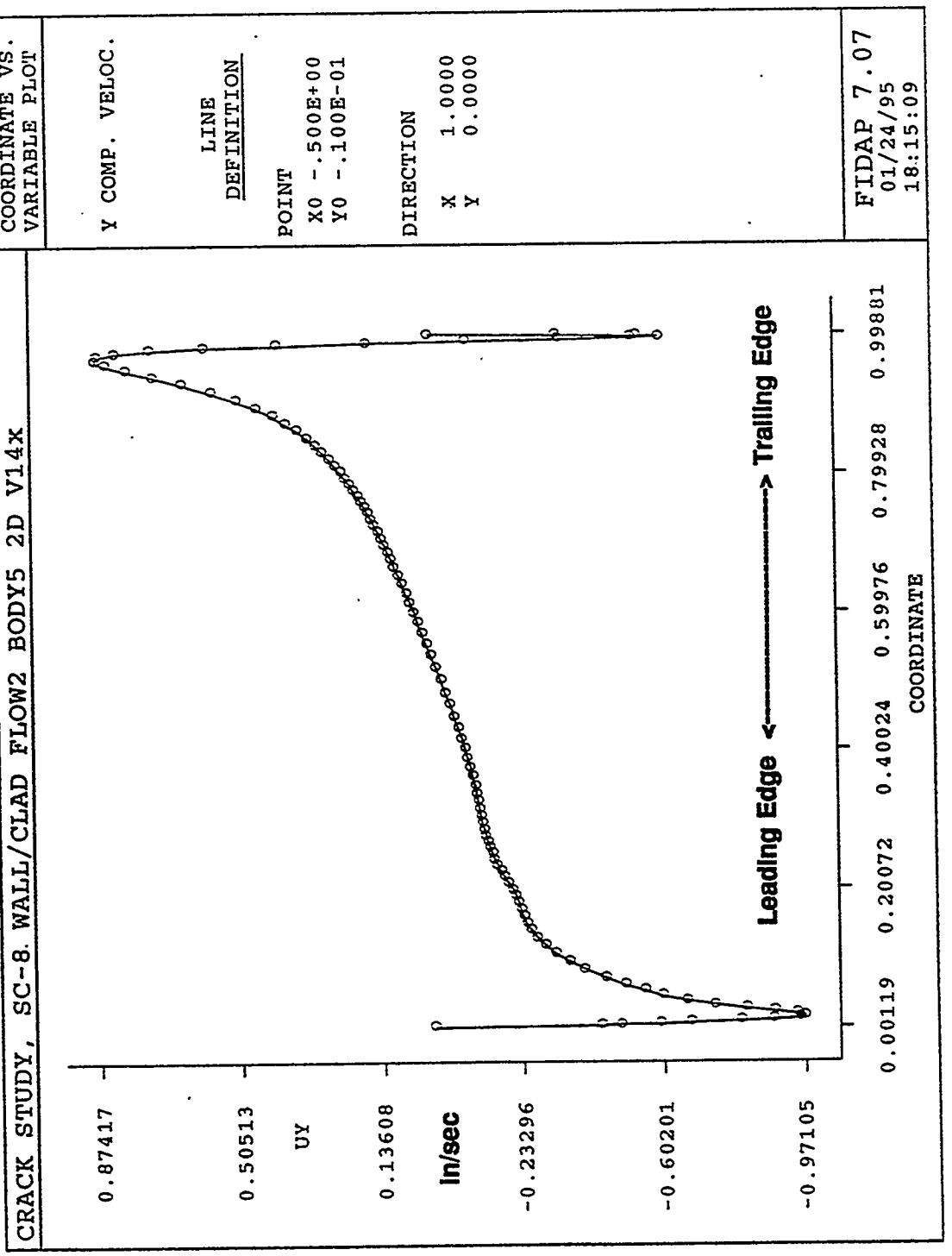

Figure 9 CFD predicted interaction pattern between the free stream and crack enclave flow fields.
Abcissa scale = inches, ordinate scale = inch/second.

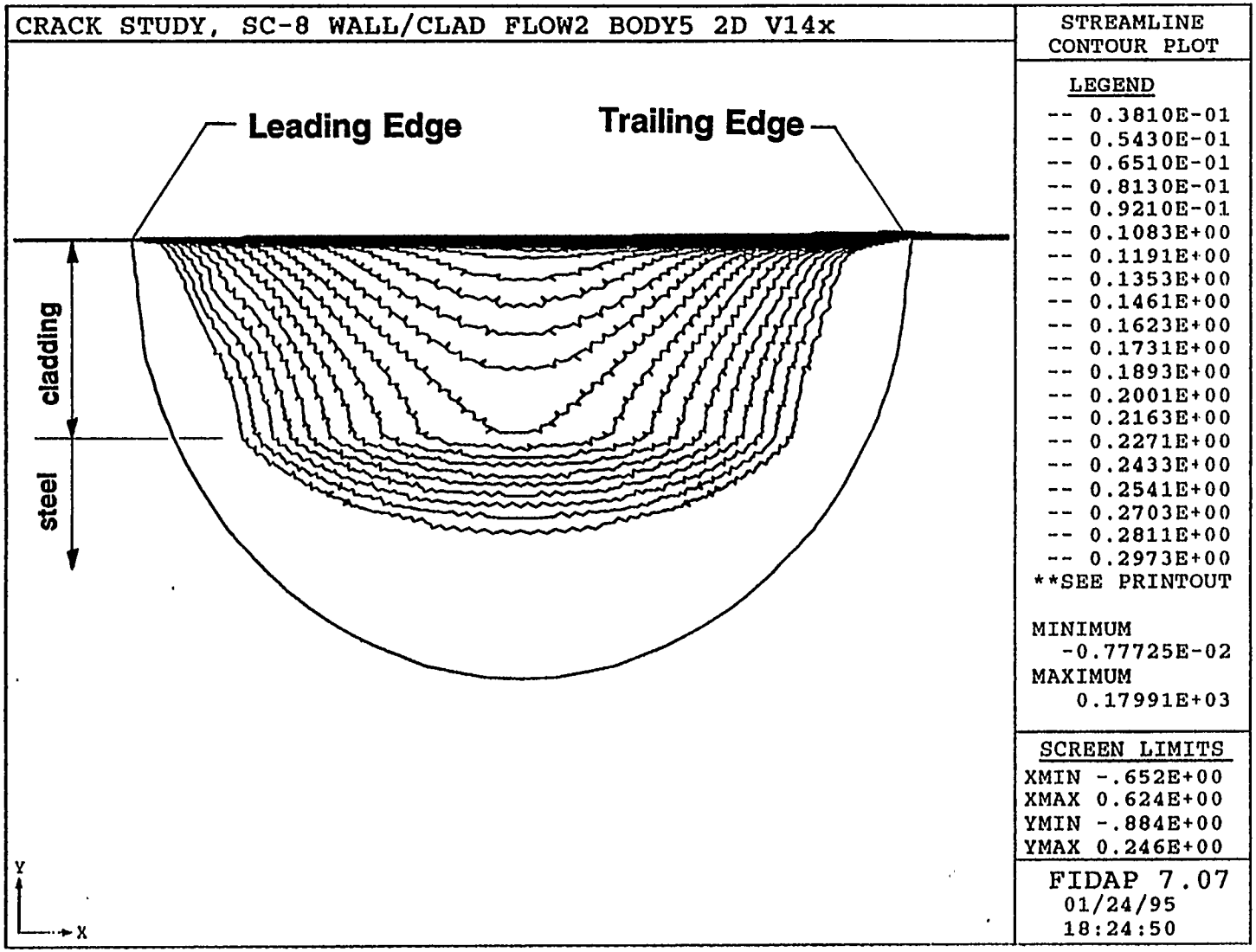

Figure 10 FIDAP calculated streamline contour plot for the crack enclave of Specimen SC-8 subjected to a mean free stream velocity of 4.74 m/sec. parallel to the crack. The direction of flow was left to right.

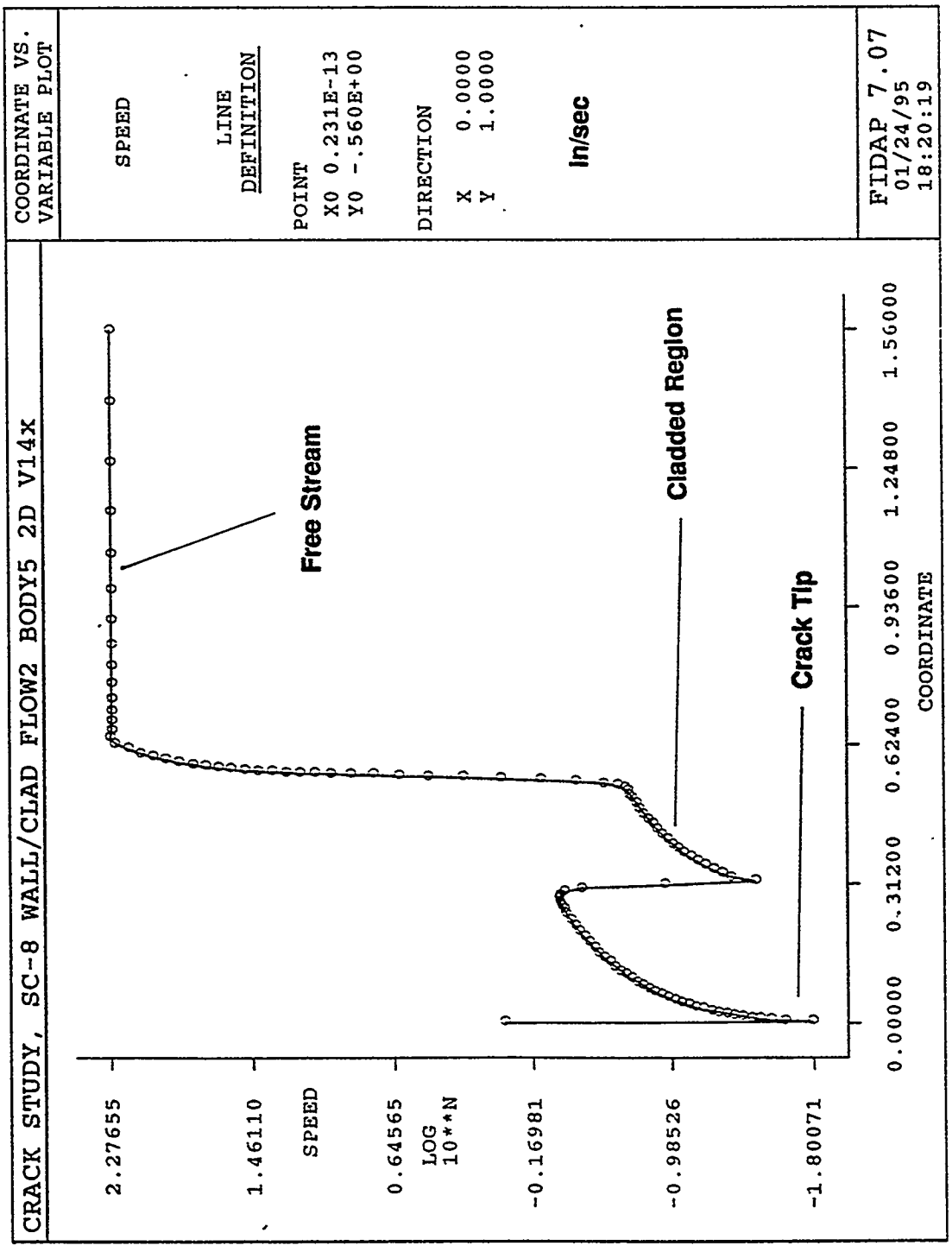

Figure 11 CFD calculated fluid velocity magnitude profile of flow in the crack enclave and the adjoining free stream for specimen SC-8. Abcissa scale = inches, ordinate scale = $\log_{10}$ (inch/second)